

A model for the wind-driven current in the wavy oceanic surface layer: apparent friction velocity reduction and roughness length enhancement

Article

Accepted Version

Teixeira, M. A. C. ORCID: <https://orcid.org/0000-0003-1205-3233> (2018) A model for the wind-driven current in the wavy oceanic surface layer: apparent friction velocity reduction and roughness length enhancement. *Journal of Physical Oceanography*, 48. pp. 2721-2736. ISSN 0022-3670 doi: 10.1175/JPO-D-18-0086.1 Available at <https://centaur.reading.ac.uk/79612/>

It is advisable to refer to the publisher's version if you intend to cite from the work. See [Guidance on citing](#).

To link to this article DOI: <http://dx.doi.org/10.1175/JPO-D-18-0086.1>

Publisher: American Meteorological Society

All outputs in CentAUR are protected by Intellectual Property Rights law, including copyright law. Copyright and IPR is retained by the creators or other copyright holders. Terms and conditions for use of this material are defined in the [End User Agreement](#).

www.reading.ac.uk/centaur

CentAUR

Central Archive at the University of Reading

Reading's research outputs online



AMERICAN METEOROLOGICAL SOCIETY

Journal of Physical Oceanography

EARLY ONLINE RELEASE

This is a preliminary PDF of the author-produced manuscript that has been peer-reviewed and accepted for publication. Since it is being posted so soon after acceptance, it has not yet been copyedited, formatted, or processed by AMS Publications. This preliminary version of the manuscript may be downloaded, distributed, and cited, but please be aware that there will be visual differences and possibly some content differences between this version and the final published version.

The DOI for this manuscript is doi: 10.1175/JPO-D-18-0086.1

The final published version of this manuscript will replace the preliminary version at the above DOI once it is available.

If you would like to cite this EOR in a separate work, please use the following full citation:

Teixeira, M., 2018: A model for the wind-driven current in the wavy oceanic surface layer: apparent friction velocity reduction and roughness length enhancement. *J. Phys. Oceanogr.* doi:10.1175/JPO-D-18-0086.1, in press.



**A model for the wind-driven current in the wavy oceanic surface layer:
apparent friction velocity reduction and roughness length enhancement**

Miguel A. C. Teixeira*

Department of Meteorology, University of Reading, Reading, United Kingdom

* *Corresponding author address:* Department of Meteorology, University of Reading, Earley Gate,

PO Box 243, Reading RG6 6BB, United Kingdom.

E-mail: m.a.teixeira@reading.ac.uk

ABSTRACT

8 A simple analytical model is developed for the current induced by the wind
9 and modified by surface wind-waves in the oceanic surface layer, based on a
10 first-order turbulence closure and including the effect of a vortex force repre-
11 senting the Stokes drift of the waves. The shear stress is partitioned between
12 a component due to shear in the current, which is reduced at low turbulent
13 Langmuir number (La_t), and a wave-induced component, which decays over
14 a depth proportional to the dominant wavelength (λ_w). The model reproduces
15 the apparent reduction of the friction velocity and enhancement of the rough-
16 ness length estimated from current profiles, detected in a number of studies.
17 These effects are predicted to intensify as La_t decreases, and are entirely at-
18 tributed to non-breaking surface waves. The current profile becomes flatter for
19 low La_t owing to a smaller fraction of the total shear stress being supported
20 by the current shear. Comparisons with the comprehensive dataset provided
21 by the laboratory experiments of Cheung and Street show encouraging agree-
22 ment, with the current speed normalized by the friction velocity decreasing as
23 La_t decreases and λ_w increases if the model is adjusted to reflect the effects
24 of a full wave spectrum on the intensity and depth of penetration of the wave-
25 induced stress. A version of the model where the shear stress decreases to zero
26 over a depth consistent with the measurements accurately predicts the surface
27 current speed. These results contribute towards developing physically-based
28 momentum flux parameterizations for the wave-affected boundary layer in
29 ocean circulation models.

30 1. Introduction

31 Flow coupling across the air-water interface in oceanic regions takes place within boundary lay-
32 ers where various properties adjust, over a relatively small fraction of the depth of the atmosphere
33 and ocean, between their values in the interior of each fluid. The atmospheric and oceanic sur-
34 face layers are the sub-layers of these boundary layers located nearest to the air-water interface,
35 occupying about 10% of their depth, which have a decisive importance in mediating the turbulent
36 fluxes of momentum, heat and gases between the atmosphere and the ocean (Csanady 2004), and
37 where these fluxes are approximately constant. Hereafter, ‘surface layer’ will always be used with
38 this meaning, although the term is often adopted in an oceanographic context to denote the whole
39 oceanic boundary layer.

40 Whereas the atmospheric surface layer over land has a no-slip bottom boundary condition ap-
41 plied at the ground, the atmospheric and oceanic surface layers in ocean regions are characterized
42 by continuity of velocity and stress at the mobile air-water interface that separates them. This, on
43 the one hand, leads to the generation of a wind-induced current in the oceanic surface layer, and
44 on the other hand allows the generation of surface waves at the air-water interface. Both of these
45 aspects considerably complicate the physics of these surface layers, especially the oceanic one, as
46 is widely recognized (Thorpe 2005) and will be further discussed here.

47 Nevertheless, the oceanic surface layer is still largely understood and modeled based on the
48 transposition to the ocean of theories developed for the atmospheric surface layer over land, where
49 the effects of surface waves are not represented (Kraus and Businger 1994). Deficiencies in this
50 approach become apparent when one realizes that key parameters in surface layer theory, such as
51 the friction velocity u_* and roughness length z_0 are deemed to take values in the ocean that seem

52 to be inconsistent with the values of the shear stress and the geometric properties of the air-water
53 interface, respectively.

54 Standard surface layer theory is based on Monin-Obukhov scaling, which in the limit of neutral
55 stratification reduces to a theory for the logarithmic mean wind profile. In the ocean, or in un-
56 derwater flows measured in the laboratory, such a theory has been applied, with varying degrees
57 of success, to model the mean current induced by the wind. However, it has often been detected
58 that the value of u_* inferred from the current profile is noticeably smaller than the one that would
59 be expected from the total shear stress (McWilliams et al. 1997, Kudryavtsev et al. 2008, Teixeira
60 and Belcher 2010), a phenomenon sometimes alternatively interpreted as an increase of the von
61 Kármán parameter (Howe et al. 1982, Cheung and Street 1988, Craig and Banner 1994, Siddiqui
62 and Loewen 2007). On the other hand, the value of z_0 obtained by extrapolating the logarithmic
63 current profile up to the surface is often much larger than would be expected based on the size of
64 the surface corrugations deforming the air-water interface, and exceeds by several orders of mag-
65 nitude the air-side value of z_0 (Csanady 1984, Burchard 2001, Soloviev and Lukas 2003, Sullivan
66 et al. 2004, Kudryavtsev et al. 2008).

67 There is some awareness that the first aspect is due to the fact that a fraction of the surface stress
68 is carried by surface waves, and therefore does not support as much shear as if the waves were
69 absent. On the other hand, the increased values of z_0 have been attributed to the effect of surface
70 waves as roughness elements seen from below, or to wave breaking, but the exact mechanism
71 by which this enhancement arises remains rather mysterious. The huge disparity between the
72 estimated values of z_0 as seen from the air-side or from the water-side of the air-water interface is
73 especially puzzling, since the amplitude of the corrugations is the same. Even if the flow on both
74 sides of the air-water interface could be assumed to be aerodynamically smooth, the differences

75 in the value of u_* between air and water would not be enough to explain the magnitude of this
76 disparity.

77 Craig and Banner (1994) and Craig (1996) developed a model of the oceanic surface layer that
78 produces profiles of the mean current and of the associated dissipation rate of turbulent kinetic
79 energy (TKE), which showed some success in predicting both quantities, and was subsequently
80 adapted and used by a number of researchers (e.g., Drennan et al. 1996, Terray et al. 1999, Gemm-
81 rich and Farmer 1999, Burchard 2001, Rascle et al. 2006, Feddersen et al. 2007, Rascle and Ard-
82 huin 2009, Gerbi et al. 2009, Kukulka and Harcourt 2017). That model is based on an approximate
83 balance between the turbulent fluxes of TKE and dissipation, and produces a substantial surface
84 dissipation enhancement, which is consistent with the observations of Gargett (1989), Agrawal
85 et al. (1992), Terray et al. (1996) and Drennan et al. (1996). However, it requires adjusting z_0
86 for each dataset, yielding values of this quantity of order the height or wavelength of the surface
87 waves, which is much larger than estimated for an aerodynamically smooth boundary, or from
88 the Charnock relation. Both Craig and Banner (1994) themselves and, more recently, Grant and
89 Belcher (2009) recognized that this need to adjust z_0 in order to fit measurements is a weakness of
90 the model.

91 More recently, Kudryavtsev et al. (2008) developed a rather elaborate model based on the mo-
92 mentum and TKE budgets, and assuming a balance between turbulence production by wave break-
93 ing and dissipation. This model avoids the strong dependence on z_0 displayed by the model of
94 Craig and Banner (1994), but contains many *ad hoc* assumptions and approximations (for exam-
95 ple, the parameterization of the TKE production by wave breaking, or the mixing length defi-
96 nition), and nevertheless is so complicated that the corresponding equations can only be solved
97 numerically. Although it predicts satisfactorily the qualitative behavior of the mean current pro-
98 files measured in the laboratory experiments of Cheung and Street (1988) and the aforementioned

99 surface dissipation enhancement, it produces dissipation profiles that look somewhat artificial and
100 seem to underestimate most datasets at small depths (see their Fig. 7). Although this model suc-
101 ceeds in predicting the enhanced values of the apparent z_0 in the experiments of Cheung and Street
102 (1988), it does not explain the reduced values of u_* that can also be inferred from the slope of the
103 mean flow profiles.

104 In this study a very simple model is developed, based on the partition of the shear stress in
105 the surface layer between shear-related and wave-related parts, that reconciles all these results,
106 explaining in particular the discrepancies between expected and observed values of u_* and z_0 in
107 the oceanic surface layer, purely due to the effect of non-breaking waves (unlike Kudryavtsev
108 et al. 2008). The model draws heavily on that developed by Teixeira (2012), which is inspired
109 by Rapid Distortion Theory (RDT) calculations, and is essentially analytical, being much simpler
110 than the one proposed by Kudryavtsev et al. (2008), but is able to produce more accurate results.
111 It has the advantage of being formulated as a variant of Monin-Obukhov scaling, where instead
112 of the Obukhov stability parameter, the key dimensionless parameters account for the effects of
113 surface waves. These parameters are the well-known turbulent Langmuir number La_t and (as
114 in Monin-Obukhov theory) a dimensionless depth, here normalized by the wavenumber of the
115 dominant surface waves. An extended version of this model was shown by Teixeira (2012) to give
116 good predictions of the dissipation rate by comparison with field data from various sources (Terray
117 et al. 1996, Drennan et al. 1996, Burchard 2001, Feddersen et al. 2007, Jones and Monismith 2008,
118 Gerbi et al. 2009). The model is tested here by comparison with the data of Cheung and Street
119 (1988), showing good agreement, despite the fact that (unlike the model of Kudryavtsev et al.
120 (2008)) it uses a monochromatic wave approximation and neglects the viscous boundary layer.

121 This paper is organized as follows: section 2 presents the proposed model, including its version
122 for a vertically uniform shear stress and its extension for a shear stress that decreases linearly with

123 depth. Section 3 contains the results, starting with tests to the model as a function of its input
124 parameters, and proceeding with its comparison with laboratory data. Finally, in section 4, the
125 main conclusions of this study are summarized.

126 **2. Theoretical Model**

127 It will be assumed that the rotation of the Earth and stratification of the water in the oceanic
128 surface layer can be neglected. The first assumption is generally acceptable in the surface layer,
129 where the flow is by definition dominated by turbulent fluxes (and throughout the whole oceanic
130 boundary layer in Equatorial regions, where the Coriolis parameter is zero). The second assump-
131 tion is acceptable if some other dynamical process (in the present case the effect of surface waves)
132 is stronger than that of buoyancy. The effect of breaking surface waves will also be neglected.
133 This is a working hypothesis, which is not as justifiable as the previous two, but was shown to be
134 a plausible approximation given the level of agreement achieved between the model of Teixeira
135 (2012) and dissipation data (for further details concerning its motivation, see that paper).

136 The water-side friction velocity u_* and roughness length z_0 will be specified according to their
137 most fundamental definitions: as the square-root of the surface value of the kinematic shear stress,
138 and as the depth at which the current velocity relative to its surface value is zero (without assuming
139 a displacement height), respectively, rather than based on the slope and intercept of the current
140 profiles (which would be misleading in the present context).

141 The point of departure for the model is that turbulence in the surface layer is dominated by the
142 transfer of kinetic energy from the mean wind-driven current and the Stokes drift of surface waves
143 to the turbulence, via the shear production and Stokes drift production terms in the TKE budget
144 (see, e.g., McWilliams et al. 1997), which are assumed to be balanced locally by the dissipation
145 rate, as in Teixeira (2011b, 2012). This balance, although of questionable accuracy, has been

146 motivated in Teixeira (2012) by the TKE budgets presented in the Large Eddy Simulation (LES)
 147 studies of Polton and Belcher (2007), Grant and Belcher (2009) and Kukulka et al. (2010) (which
 148 did not account for the effects of wave breaking). More recent supporting evidence for this balance
 149 is provided by Van Roekel et al. (2012) and Kukulka and Harcourt (2017).

150 RDT studies (e.g. Lee et al. 1990, Teixeira and Belcher 2002, Teixeira and Belcher 2010, Teix-
 151 eira 2011a) have indicated that the characteristics of the turbulence (i.e., its anisotropy and rate
 152 of energy transfer from the mean flow) are determined by its distortion by the mean current shear
 153 dU/dz (where $U(z)$ is the mean current speed), which promotes horizontal ‘streaky structures’,
 154 and by the Stokes drift gradient dU_S/dz (where $U_S(z)$ is the Stokes drift velocity), which promotes
 155 instead streamwise vortices with strong vertical velocity fluctuations. The influence of surface
 156 waves can be measured by the relative importance of these two strain rates, since the correspond-
 157 ing production terms in the TKE budget may be written (for a wind stress aligned in the x direction)

$$-\overline{u'w'}\frac{dU}{dz}, \quad -\overline{u'w'}\frac{dU_S}{dz}, \quad (1)$$

158 where $\tau/\rho = -\overline{u'w'}$ is the kinematic shear stress (with u' and w' being the horizontal and vertical
 159 turbulent velocity fluctuations, respectively) and ρ is the density. It will be assumed hereafter that
 160 dU/dz and dU_S/dz have the same sign (> 0), which is the typical situation for wind-driven waves.

161 *a. Scaling of the oceanic surface layer*

162 The vertical gradient of the Stokes drift of a deep-water monochromatic surface wave of ampli-
 163 tude a_w , wavenumber k_w and angular frequency σ_w at a depth z is given by (Phillips 1977)

$$\frac{dU_S}{dz} = 2(a_w k_w)^2 \sigma_w e^{-2k_w |z|}, \quad (2)$$

164 and, to a first approximation, in the surface layer the mean current shear satisfies

$$\frac{dU}{dz} = \frac{u_*}{\kappa |z|}, \quad (3)$$

where κ is the von Kármán constant. To evaluate the relative importance of the Stokes drift strain rate and mean shear rate of the current, the ratio of (2) and (3) may be taken at a representative depth where the flow is affected by surface waves, say $|z| = 1/(2k_w)$, yielding

$$R = \frac{dU_S/dz}{dU/dz}(|z| = 1/(2k_w)) = \kappa e^{-1} (a_w k_w)^2 \frac{c_w}{u_*} = \kappa e^{-1} \frac{U_S(z=0)}{u_*} = \kappa e^{-1} La_t^{-2}, \quad (4)$$

where $U_S(z=0) = (a_w k_w)^2 c_w$ is the Stokes drift velocity at the surface, $c_w = \sigma_w/k_w$ is the phase speed of the waves, and $La_t = (u_*/U_S(z=0))^{1/2}$ is the turbulent Langmuir number. Incidentally, $|z| = 1/(2k_w)$ is also the depth at which R attains its maximum (cf. Teixeira and Belcher 2010, Teixeira 2011a).

Consider first the magnitude of R in the atmosphere. Although one does not often think about Stokes drift in the atmosphere, its magnitude is similar to that in the ocean, since the wave orbital motions (usually immersed in a tangle of turbulent eddies) are likewise of similar magnitude. dU_S/dz is estimated here as if dU/dz did not affect the wave motion, which is certainly not strictly true, but provides a leading-order approximation. For waves of slope $a_w k_w \approx 0.1$ and wavelengths in the range $\lambda_w \approx 1 - 100$ m, taking into account that $k_w = 2\pi/\lambda_w$, then the wavenumber is in the range $k_w \approx 0.06 - 6.3 \text{ m}^{-1}$, and using the linear dispersion relation of deep-water gravity waves, $c_w = \sqrt{g/k_w}$, one obtains $c_w \approx 1.25 - 12.5 \text{ m s}^{-1}$, with the limits swapped relative to those of k_w . Taking a typical value of the friction velocity in the atmosphere, $u_* \approx 0.3 \text{ m s}^{-1}$, (4) yields $R \approx 6 \times 10^{-3} - 6 \times 10^{-2}$ (where $\kappa = 0.4$ was assumed), which is very small. This means, perhaps unsurprisingly, that the effect of the Stokes drift in the atmosphere is fairly insignificant, and the surface layer should be dominated by mean wind shear.

For the oceanic surface layer, although the same estimates for the wave characteristics may be used, it must be noted that, to a first approximation, the shear stress τ is continuous across the air-water interface in steady flow, and since by definition $\overline{u'w'}(z=0) = -u_*^2$, then ρu_*^2 must be

continuous at that interface. Given that the density ratio between water and air is ≈ 833 , the friction velocity in the water will be smaller by a factor of $\sqrt{833} \approx 29$. This gives a typical friction velocity of $u_* \approx 0.01 \text{ ms}^{-1}$, yielding $R \approx 0.17 - 1.7$, which is of $O(1)$. In reality, the value of u_* used in (3) should be even smaller, since part of the shear stress is supported by the wave as well as by the mean shear (as will be seen later), so that it is common to have R substantially higher than 1. In addition, it is quite possible that $a_w k_w > 0.1$, which also increases R . This means that in the ocean it is unacceptable to ignore the effect of the Stokes drift of surface waves, and this difference is what gives oceanic turbulence its distinctive character, as shown by McWilliams et al. (1997) using LES and Teixeira and Belcher (2002, 2010) and Teixeira (2011a) using RDT.

b. Shear stress partition

The Craik-Leibovich equations including the effect of the Stokes drift of surface waves may be manipulated, in the same way as done for obtaining a TKE budget including the production terms (1), to obtain an equation for evolution of the shear stress (Teixeira 2011a):

$$\frac{d}{dt} \overline{u'w'} = -\overline{w'^2} \frac{dU}{dz} - \overline{u'^2} \frac{dU_S}{dz} + \text{other terms.} \quad (5)$$

This equation shows that the shear stress receives contributions proportional to the mean shear and to the Stokes drift strain rate. This prompted Teixeira (2011a) to decompose $\overline{u'w'}$ into shear-induced and wave-induced components, proportional to the corresponding production terms explicitly presented in (5). Hence, the shear-induced component of $\overline{u'w'}$ can be parameterized as

$$(\overline{u'w'})_s = \overline{u'w'} \frac{\overline{w'^2} dU/dz}{\overline{w'^2} dU/dz + \overline{u'^2} dU_S/dz} = \frac{\overline{u'w'}}{1 + \frac{\overline{u'^2} dU_S/dz}{\overline{w'^2} dU/dz}} = \frac{\overline{u'w'}}{1 + \frac{\overline{u'^2}}{\overline{w'^2}} 2\kappa (a_w k_w)^2 \frac{c_w}{u_*} k_w |z| e^{-2k_w |z|}}, \quad (6)$$

where (2) and (3) have been used. Although the logarithmic current profile is modified by wave effects (as shown in the following section) and therefore (3) is not strictly accurate, it provides a correct scaling which makes the proposed shear stress partition both be simple enough and benefit

from good properties. The inaccuracy of this approximation is likely to partially cancel with those of other adopted assumptions, as noted below. Using the definitions of u_* , $U_S(z=0)$ and La_t , (6) may be alternatively expressed as

$$(\overline{u'w'})_s = -\frac{u_*^2}{1 + 2\kappa \frac{\overline{u'^2}}{w'^2} \frac{U_S(z=0)}{u_*} k_w |z| e^{-2k_w |z|}} = -\frac{u_*^2}{1 + 2\kappa \frac{\overline{u'^2}}{w'^2} La_t^{-2} k_w |z| e^{-2k_w |z|}}, \quad (7)$$

where it has been noted that in the surface layer the shear stress $\overline{u'w'}$ is constant and equal to $-u_*^2$. If, following Teixeira (2012), it is assumed that the quantity $\gamma = 2\kappa(k_w |z|) \frac{\overline{u'^2}}{w'^2}$ is approximately constant (which has some plausibility given that $\overline{w'^2}$ must approach zero as $z \rightarrow 0$, particularly in a curvilinear wave-following coordinate system – cf. Teixeira and Belcher (2002)), then the shear-induced shear stress takes the form

$$(\overline{u'w'})_s = -\frac{u_*^2}{1 + \gamma La_t^{-2} e^{-2k_w |z|}}, \quad (8)$$

where γ is an adjustable (positive) coefficient. The calibration of this coefficient may be exploited to account for extraneous effects, such as the possibility that the waves are non-monochromatic, and the fact that the current profile is not perfectly logarithmic. Assuming that γ is constant with depth is likely to be less accurate outside the surface layer, because the above assumptions about the behavior of $\overline{w'^2}$ and dU/dz as $z \rightarrow 0$ do not hold anymore, but the model is not applicable there anyway.

Note that (8) has the properties of approaching the usual definition of the total shear stress as either $|z| \rightarrow \infty$ or $La_t \rightarrow \infty$, both of which make sense physically. The usual wall-layer scaling for the dissipation rate, consistent with (3) and with a logarithmic current profile, was shown to hold by the observations of various authors at sufficiently large depths (Gargett 1989, Agrawal et al. 1992, Terray et al. 1996), and is obviously recovered when the influence of surface waves becomes vanishingly small (which corresponds to $La_t \rightarrow \infty$) (McLeish and Putland 1975, Kondo 1976). The remaining part of the shear stress, $\overline{u'w'} - (\overline{u'w'})_s$, is evidently wave-related, and ap-

proaches zero when either $|z| \rightarrow \infty$ or $La_t \rightarrow \infty$. Its depth of penetration is clearly, from (8), of $O(1/(2k_w))$, although it should be borne in mind that this particular dependence results directly from the monochromatic wave approximation. Other approaches to treat the dependence of $(dU_S/dz)/(dU/dz)$ (as well as that of $\overline{u'^2}/\overline{w'^2}$) with depth could result in different functional forms for $(\overline{u'w'})_s$, with γ possibly not being treated as a constant.

An interesting property of (8) is that, when evaluated at the surface, it allows the definition of a modified friction velocity affected by shear, u_{*S} , as

$$u_{*S} = -\frac{(\overline{u'w'})_s}{u_*} = \frac{u_*}{1 + \gamma La_t^{-2}}. \quad (9)$$

Clearly, u_{*S} is always smaller than u_* , and can even become much smaller when La_t is low. This is in agreement with LES results by, e.g., McWilliams et al. (1997), Li et al. (2005) and Grant and Belcher (2009) showing that shear in the current profile decreases markedly for a constant wind stress τ as La_t decreases (see section 3). One advantage of (9) is that it allows the definition of friction velocities due to shear and due to the wave that are additive, yielding the sum u_* . The present approach partially resembles the modification of the surface shear stress to account for wave effects in the study of the Ekman-Stokes boundary layer by Polton et al. (2005), where, however, the Earth's rotation effect was taken into account.

c. A model for the current profile

To obtain a model for the current profile that is consistent with the existing surface layer theory, a first-order turbulence closure is applied to the shear-related shear stress, namely

$$(\overline{u'w'})_s = -K_m \frac{dU}{dz}, \quad (10)$$

where $K_m = \kappa u_* |z|$, as usually defined. Here u_* is taken as the relevant velocity scale for momentum transport, since the vertical velocity fluctuations, which effect this transport, scale on u_* rather

248 than on u_{*s} . Then the shear of the mean current can be expressed as

$$\frac{dU}{dz} = -\frac{(\overline{u'w'})_s}{\kappa u_* |z|} = \frac{u_*}{\kappa |z|} \phi_L(La_t, k_w |z|), \quad (11)$$

249 where (8) has been used in the second equality, and

$$\phi_L(La_t, k_w |z|) = \frac{1}{1 + \gamma La_t^{-2} e^{-\varepsilon k_w |z|}}, \quad (12)$$

250 where $\varepsilon = 2$ from (8), but will hereafter be kept as an adjustable parameter for maximum gener-
 251 ality. As for γ , the adjustment of ε may be exploited to account for various extraneous effects,
 252 such as the presence of non-monochromatic waves. The connection with this latter aspect is even
 253 closer, since ε controls the vertical penetration of wave effects, which may depend not only on the
 254 dominant wavelength, but also on the wave energy distribution by scale.

255 Note that ϕ_L plays in (11) a role analogous to that played by stability functions in Monin-
 256 Obukhov theory of the non-neutral surface layer. The difference resides in the fact that ϕ_L depends
 257 on wave quantities (according to (12)) instead of on stratification. This formulation is amenable to
 258 improvement, since the form of (12) only needs to be modified to account for missing effects or
 259 a more accurate representation of the effects already considered. The form taken by (11) implies
 260 that both at large depths (where usual surface layer scaling is recovered) and near the surface $z \approx 0$
 261 the current profile is approximately logarithmic, but with different friction velocities u_* and u_{*s} ,
 262 respectively, as expressed by (9). The dependence of (12) on z is, arguably, the simplest possible
 263 that benefits from these properties. The partition of the shear stress into shear-induced and wave-
 264 induced components, conjugated with the use of a first-order turbulence closure (10), parallels the
 265 approach, used in a numerical modeling context, of Harcourt (2013). However, the partition itself
 266 was originally suggested by Teixeira (2011a) based on the shear stress budget (5), and used in the
 267 present form by Teixeira (2012).

From (10), (11) and (12) it is possible to define an ‘effective’ eddy viscosity K_m^* that takes into account wave effects:

$$K_m^* = -\frac{\overline{u'w'}}{dU/dz} = \kappa u_* |z| \left(1 + \gamma La_t^{-2} e^{-\varepsilon k_w |z|} \right). \quad (13)$$

Its form clearly shows the apparent mixing enhancement resulting from the reduction of dU/dz .

To complete the model, it remains to integrate (11) between $z = z_0$ (where $U = U_0$, U_0 being the Eulerian current at the surface), and a generic z . This yields

$$U_0 - U(z) = \frac{u_*}{\kappa} \int_{z_0}^{|z|} \frac{1}{z'} \frac{1}{1 + \gamma La_t^{-2} e^{-\varepsilon k_w z'}} dz'. \quad (14)$$

If velocities are normalized by u_* and $|z|$ by k_w , (14) may be rewritten

$$\frac{U_0 - U(z)}{u_*} = \frac{1}{\kappa} \int_{k_w z_0}^{k_w |z|} \frac{1}{z'} \frac{1}{1 + \gamma La_t^{-2} e^{-\varepsilon z'}} dz'. \quad (15)$$

Often, current profiles in the surface layer are specified using so-called wall-coordinates, defined as $U^+ = (U_0 - U(z))/u_*$ and $z^+ = |z|u_*/\nu$, where ν is the kinematic viscosity of water. Using these definitions, (15) can be expressed as

$$U^+ = \frac{1}{\kappa} \int_{\frac{k_w \nu}{u_*} \frac{z_0 u_*}{\nu}}^{\frac{k_w \nu}{u_*} z^+} \frac{1}{z'} \frac{1}{1 + \gamma La_t^{-2} e^{-\varepsilon z'}} dz'. \quad (16)$$

The advantage of expressing the lower limit of integration in this form is that for aerodynamically smooth flow, $z_0 u_*/\nu = 0.11$ (Cheung and Street 1988, Kraus and Businger 1994), a result that will be used below. The integral in (15) or (16) cannot in general be evaluated analytically. For numerical evaluation purposes only, it is useful to introduce the further change of variable $z' = \exp \zeta$, which transforms (16) into

$$U^+ = \frac{1}{\kappa} \int_{\log(\frac{k_w \nu}{u_*} \frac{z_0 u_*}{\nu})}^{\log(\frac{k_w \nu}{u_*} z^+)} \frac{1}{1 + \gamma La_t^{-2} e^{-\varepsilon \exp \zeta}} d\zeta. \quad (17)$$

This eliminates the singularity at $z' = 0$, which is especially bothersome for small values of z_0 .

In the limit $La_t \rightarrow \infty$, (17) (or (16)) can, of course, be integrated analytically, reducing to

$$U^+ = \frac{1}{\kappa} \log \left(\frac{z^+ \mathbf{v}}{z_0 u_*} \right) = \frac{1}{\kappa} \log \left(\frac{|z|}{z_0} \right). \quad (18)$$

For aerodynamically smooth flow, (18) further reduces to

$$U^+ = \frac{1}{\kappa} \log \left(\frac{z^+}{0.11} \right) = \frac{1}{\kappa} \log z^+ + 5.5, \quad (19)$$

as noted by Cheung and Street (1988), where it was assumed that $\kappa = 0.4$.

When plotted with a logarithmic scale for depth, (17) consists of two straight line segments separated by a transition depth interval centered around $|z| \approx 1/(\epsilon k_w)$. The slope of the current profile in its upper, wave-affected part, is consistent with the reduced friction velocity u_{*s} , given by (9), i.e.,

$$\frac{dU}{dz}(z \rightarrow 0) = \frac{u_{*s}}{\kappa|z|} \quad (20)$$

(as results from (9), (11) and (12)), and u_* is of course consistent with the slope of the profile segment occurring at larger depths (see discussion below). The roughness length z_0 is the height at which $U^+ = 0$, irrespective of whether the current profile is affected by waves or not. In the latter case, an apparent roughness length can be defined, which corresponds to the intersect of the prolongation of the segment of the current profile at large depths with the axis where $U^+ = 0$. It can be anticipated that this apparent roughness length z_{0w} is much larger than the true z_0 when the effect of waves is important, because of the break point (or more precisely transition region) existing in the current profile. z_{0w} can be obtained by integrating (11) between z_0 and ∞ and then (3) back to z_{0w} . This yields

$$\log(k_w z_{0w}) = \log(k_w z_0) + \gamma La_t^{-2} \int_{\log(k_w z_0)}^{\infty} \frac{e^{-\epsilon \exp \zeta}}{1 + \gamma La_t^{-2} e^{-\epsilon \exp \zeta}} d\zeta. \quad (21)$$

Equations (9), (17) and (21) form the basis of the calculations presented in this paper.

It is worth noting that the formulation of the shear stress on which these equations are based, (10), is strictly local, neglecting any transport effects, whereby dU/dz might become negative with $\overline{u'w'}$ remaining also negative (corresponding to a negative eddy viscosity in (10)). This behavior, which is produced in a number of LES results (McWilliams et al. 1997, Li et al. 2005, Tejada-Martinez et al. 2013), was recently parameterized by Sinha et al. (2015) by adopting a non-local component of the shear stress, akin to those used in momentum flux parameterizations for convection. Since the data used in the present study (from Cheung and Street 1988) do not show such negative current shear (another example is the top surface layer in Fig. 5 of Longo et al. (2012)), that approach is not used here, although it may be viewed as one of the possible improvements to the present scheme.

1) MODEL FOR A LINEARLY DECREASING SHEAR STRESS

For the purpose of comparing the model developed above with the laboratory measurements of Cheung and Street (1988) (to be done below), it is convenient to assume that the shear stress is not constant with depth, but rather varies linearly from its maximum at the air-water interface to zero at a certain depth. This parallels the approach used by Cheung and Street (1988) to estimate the shear stress from their data, and corresponds mathematically to

$$\overline{u'w'} = -u_*^2 \left(1 - \frac{|z|}{\delta}\right) \quad \text{if } |z| \leq \delta, \quad (22)$$

where δ is the depth where $\overline{u'w'}$ becomes zero, and it is implied that for $|z| > \delta$, $\overline{u'w'} = 0$. In this case, the function ϕ_L must be redefined (for $|z| \leq \delta$) as

$$\phi_L \left(La_t, k_w |z|, \frac{|z|}{\delta} \right) = \frac{1 - \frac{|z|}{\delta}}{1 + \gamma La_t^{-2} e^{-\varepsilon k_w |z|}}, \quad (23)$$

and (11) may then be integrated to give

$$U^+ = \frac{1}{\kappa} \int_{\frac{k_w v}{u_*}}^{\frac{k_w v}{u_*} z^+} \left(\frac{1}{z'} - \frac{1}{k_w \delta} \right) \frac{1}{1 + \gamma La_t^{-2} e^{-\varepsilon z'}} dz' \quad (24)$$

319 (again valid only for $|z| \leq \delta$), replacing (16). For $|z| > \delta$, $U^+ = U^+(z^+ = \delta u_*/v)$, which is a
 320 constant. In the limit $La_t \rightarrow \infty$, (24) reduces to

$$U^+ = \frac{1}{\kappa} \left[\log(z^+) - \frac{z^+}{\frac{\delta u_*}{v}} - \log\left(\frac{z_0 u_*}{v}\right) + \frac{z_0}{\delta} \right], \quad (25)$$

321 which has a log-linear variation and must replace (19).

322 Note that, according to (10) and (22), for $|z| > \delta$, $dU/dz = 0$ under the present assumptions,
 323 i.e., no mean shear exists and the current speed does not vary. This gives the version of the model
 324 just described the capability of predicting the surface value of the wind-induced current (unlike
 325 the version described in the previous subsection, where U varies indefinitely). Defining arbitrarily
 326 $U(|z| = \delta) = 0$, which makes sense since this is the value of the current at the depth where the
 327 effect of the surface wind stress is no longer felt, then from the definition of U^+ it follows that
 328 $U_0/u_* = U^+(|z| = \delta) = U^+(z^+ = \delta u_*/v)$, which can be obtained from (24).

329 As a caution, it should be emphasized that the assumption of a non-constant shear stress, ex-
 330 pressed by (22), may not be strictly consistent with statistically steady and horizontally homoge-
 331 neous flow (implicit in surface layer theory), requiring either a time evolution of the mean current
 332 or a mean horizontal pressure gradient, but hopefully this assumption is still acceptable for the
 333 present purposes. A model with a linearly decreasing shear stress, such as the one just presented,
 334 might be thought of as a very simple representation of the whole oceanic boundary layer (of depth
 335 δ) instead of just the surface layer. However, its applicability to real cases is limited by neglect
 336 of the effect of the Earth's rotation, the choices made to approximate (7) as (8), and the Monin-
 337 Obukhov approach inherent to (11) and (12). These are confined to the surface layer, and would
 338 require modification in order to extend the model.

3. Results

It is instructive first of all to explore the model behavior for a few representative cases, because this illustrates in the ‘cleanest’ possible way the range of behavior of the model and its impact on the perceived values of the water-side values of u_* and z_0 . More detailed comparisons with laboratory experiments follow. In all of these cases, γ and ε will be treated as adjustable parameters.

a. Generic behavior of the model

Figure 1 shows profiles of U^+ as a function of $k_w|z|$ from (15) for $k_w z_0 = 0.001$ and different values of the turbulent Langmuir number $La_t = 0.5, 1, 2$, assuming that $\gamma = 1$ and $\varepsilon = 1$, for simplicity. Note that these values of γ and ε are of the same order of magnitude as those adopted by Teixeira (2012). The results are not qualitatively very sensitive to $k_w z_0$ in the representation adopted in Fig. 1, and variation of this parameter merely leads to a rescaling of the horizontal axis, with a narrower transition region between the two logarithmic portions of the curves occurring for values of $k_w z_0 \ll 1$.

$La_t = 2$ intends to represent shear-dominated turbulence, $La_t = 0.5$ Langmuir (i.e., wave-dominated) turbulence, and $La_t = 1$ turbulence with a transitional character. As can be seen in Fig. 1, the current profiles (denoted by the solid curves) have a lower portion with invariant slope for larger depths. This slope, when expressed in terms of $U^+/\log|z|$, is $1/\kappa$, because of the way U^+ is normalized. At smaller depths the current profile has a lower slope (prolonged to larger $|z|$ as the dashed asymptotes), which is proportional to the values of the ratio u_{*s}/u_* in each case. From (9) (for $\gamma = 1$), these values are $u_{*s}/u_* = 0.8$ for $La_t = 2$, $u_{*s}/u_* = 0.5$ for $La_t = 1$ and $u_{*s}/u_* = 0.2$ for $La_t = 0.5$. On the the other hand, if the lower portion of the current profile is prolonged towards the surface (dotted line asymptotes), one obtains an “effective” value of the roughness length, expressed by (21), which would be obtained by ignoring the upper portion of the current profile. For

362 $La_t = 2$, $k_w z_{0w} = 0.004$, for $La_t = 1$, $k_w z_{0w} = 0.030$ and for $La_t = 0.5$, $k_w z_{0w} = 0.341$, which shows
363 dramatically how z_{0w} may become various orders of magnitude larger than z_0 as La_t decreases (see
364 further discussion below).

365 Note that, according to the present model, if measurements are taken at a range of depths well
366 below the transition region located around $|z| \approx 1/(\epsilon k_w)$, the friction velocity corresponding to
367 the total momentum flux u_* will be diagnosed correctly from the current profile, but the roughness
368 length z_0 will be strongly overestimated as z_{0w} . Conversely, if measurements are taken at a range
369 of depths above this transition region (if that is feasible), z_0 will be correctly diagnosed from the
370 current profile, but u_* will be underestimated as u_{*s} . Data taken from an intermediate depth range
371 coinciding with the transition between the two asymptotic portions of the profile (if they form a
372 reasonably straight line in a logarithmic scale) will lead both to an overestimation of z_0 and to an
373 underestimation of u_* . It is likely that at least one of these three possibilities occurs in a large
374 fraction of the available field or laboratory measurements of wave-affected mean currents.

375 Circumstantial evidence that this is so is provided by the reported need to change (more specifi-
376 cally decrease) the value of the von Kármán constant to achieve an adequate collapse of measured
377 current profiles in wall coordinates (Howe et al. 1982, Cheung and Street 1988, Craig and Banner
378 1994, Siddiqui and Loewen 2007), unless the friction velocity used to define U^+ is that diagnosed
379 from the current profile itself, here defined as u_{*s} (Siddiqui and Loewen 2007), which masks this
380 problem. Clearly, neither of these procedures is very satisfactory, given their arbitrariness. More
381 evidence supporting the discussion in the preceding paragraph is provided by the consistently high
382 reported values of the roughness length diagnosed from current profiles, exceeding by orders of
383 magnitude the value that would be expected from the morphology of the air-water interface, or
384 the flow regime (Csanady 1984, Burchard 2001, Soloviev and Lukas 2003, Sullivan et al. 2004,
385 Kudryavtsev et al. 2008)). Yet more indications, of a more doubtful but suggestive nature, are

provided by the fact that the slope of wave-affected currents plotted in wall-layer coordinates increases in some cases at larger depths (see, e.g., the diamond and circle symbols in Fig. 1 of Cheung and Street (1988), or the black circles and diamonds in Fig. 6 of Siddiqui and Loewen (2007)).

Although both a decrease of the friction velocity and an increase of the roughness length, as diagnosed from current profiles, might be expected as a result of vertical mixing of momentum due to wave breaking, the remarkable property of the model proposed here is that this phenomenon arises simply due to the partition of the shear stress imposed by non-breaking waves, something that can be traced back to the production terms of the shear stress budget (5), and is thus much easier to pinpoint physically. It is, of course, possible, and even likely, that both processes act in concert when wave breaking does occur, but it is striking that the present mechanism does not require wave breaking.

Figure 2 shows the variation of u_{*s}/u_* as a function of La_t for different values of the calibrating constant γ , from (9). Unsurprisingly, this ratio takes values that range from ≈ 1 for large La_t to $\ll 1$ for small La_t . Clearly, what matters for a correct representation of the variation in between is the value of γ , with large values corresponding to strong wave effects and small values to weaker wave effects. This partition of the friction velocity, or between the corresponding shear-induced and wave-induced stresses, is not an often measured or calculated quantity, but Fig. 5 of Bourassa (2000) presents an example with some relevance, even if a quantitative comparison is not easy. If an increase in wind speed is equated with a decrease of La_t (an idea that is suggested by the comparisons of the next subsection), and the ratio of the aqueous shear stress to the total atmospheric stress is equated with u_{*s}/u_* (which must at least be partially correct because the aqueous stress is estimated from current profiles), the decreasing trend of this ratio with increasing wind speed in Fig. 5 of Bourassa (2000) is consistent with Fig. 2. Another aspect that suggests this reasoning

410 is sound is the leveling off of the stress ratio for the highest wind speeds in Fig. 5 of Bourassa
 411 (2000). This is clearly consistent with a smaller sensitivity of La_t to the wind speed at the highest
 412 wind speeds, which is corroborated by the comparisons presented in the next subsection. Both
 413 results are compatible with the established idea that in well-developed seas in the real ocean, La_t
 414 becomes largely independent of the wind speed.

415 Figure 3 presents the variation of $k_w z_{0w}$ and z_{0w}/z_0 as a function of La_t from (21) for $\gamma = 1$
 416 and $\varepsilon = 1$ (as assumed in Fig. 1) and different values of $k_w z_0$. As expected, $k_w z_{0w}$ approaches
 417 $k_w z_0$ for large values of La_t , but tends to a value independent of $k_w z_0$ at small La_t . What this
 418 means is that at low La_t , z_{0w} scales with k_w^{-1} rather than with z_0 , i.e., z_{0w} is proportional to the
 419 wavelength of the dominant waves, not to any property of small-scale capillary waves (neglected
 420 in the model), or to the amplitude of the dominant waves a_w . This behavior is confirmed by the
 421 ratio z_{0w}/z_0 , which only approaches 1 for large values of La_t , whereas it tends to be very high for
 422 small La_t . As is consistent with the behavior of $k_w z_{0w}$, z_{0w}/z_0 at low La_t is inversely proportional
 423 to $k_w z_0$. Since in real situations $k_w z_0$ may easily be as small as 10^{-5} , the amplification of the
 424 apparent roughness length can be very pronounced. A qualitative comparison with Fig. 3 of
 425 Bourassa (2000) is pertinent. Although the dependence of z_0 (which should probably be taken
 426 as z_{0w} in the present notation) with u_* in that figure cannot be tested quantitatively because wave
 427 information is missing, and the dependence on u_* affects both the true value of z_0 (see (26) below)
 428 and (21) via the definition of La_t , the important point to retain from Fig. 3 of Bourassa (2000) is
 429 the enormous amplification of z_0 . Bourassa (2000) notes that z_0 is about 10^5 larger than expected
 430 from Charnock's relation (and therefore much higher than the values estimated for the true z_0 in
 431 the next subsection).

432 *b. Comparison with Cheung et al. (1988)*

433 Finding adequate datasets to test the present model is challenging, because usually the quantities
434 required as input to the model are not measured. First of all, measuring current profiles in the field
435 with the required accuracy is extremely difficult, hence the most relevant studies typically involve
436 laboratory experiments. Even in those cases, almost invariably not all relevant wave quantities
437 are measured (Bourassa 2000, Siddiqui and Loewen 2007, Longo et al. 2012), and often the shear
438 stress is not measured directly, but rather estimated from the current profiles (Bourassa 2000,
439 Siddiqui and Loewen 2007), which makes comparisons more difficult (the erratic behavior of the
440 current speeds measured by Siddiqui and Loewen (2007) as a function of the wind speed is another
441 reason to exclude their data). A notable exception are the laboratory experiments of Cheung and
442 Street (1988) of the current beneath surface waves generated by the wind. The relevant quantities
443 are presented in their Table 1. As Kudryavtsev et al. (2008) do for the comparison presented in
444 their Fig. 10, only wind-generated waves are considered here and the case among these waves
445 with the lowest wind-speed (where the wave amplitude is so small as to be barely measurable) is
446 ignored.

447 The experiments with mechanical waves are excluded from this comparison because the assump-
448 tion of the model that dU/dz and dU_S/dz have the same sign may not be strictly satisfied. The
449 possibility that dU/dz and dU_S/dz have opposite signs has been demonstrated by Pearson (2018),
450 for situations with weak (or no) wind, when turbulence exists beneath a wave field. This leads to
451 a suppression of the instability to Langmuir circulations (which requires $(dU/dz)(dU_S/dz) > 0$),
452 modifying the stress partition assumed in (8), which relies on the existence of that instability
453 (Teixeira 2011a).

For a reasonable range of input parameters, the present model predicted almost no difference between the current profiles beneath wind waves for the two lowest wind speeds in Table 1 of Cheung and Street (1988). This justifies (following Kudryavtsev et al. (2008)) ignoring the profile for the lowest wind speed, 1.5 m s^{-1} , which has a roughness length smaller than that expected for an aerodynamically smooth flow, and might be affected by some inaccuracy.

1) UNBOUNDED MODEL

The first comparison to be made uses an uncalibrated version of the ‘unbounded’ model described in section 2c. The values of u_* from Table 1 of Cheung and Street (1988) are used directly in the model, the wave orbital velocity $a_w k_w c_w$ is taken as $\sqrt{2}(\bar{u}_0^2)^{1/2}$, where $(\bar{u}_0^2)^{1/2}$ is the root-mean-square orbital velocity in the data (as is consistent with Eqs. (4)-(5) of Cheung and Street (1988), where $\hat{\eta}_S$ is equivalent to a_w here), the angular frequency σ_w is equated to $2\pi f_D$, where f_D is the frequency (in cycles) of the dominant waves, and the corresponding wavenumber is $k_w = \sigma_w^2/g$ from the linear dispersion relation of deep-water surface gravity waves. Some key parameters are presented in Table 1. An evidently crucial detail is how to define z_0 . As a first approximation the definition valid for aerodynamically smooth flow is adopted: $z_0 = 0.11\nu/u_*$ (Kraus and Businger 1994), with $\nu = 10^{-6} \text{ m}^2 \text{ s}^{-1}$. Figure 4 shows a comparison of the model with the data presented in Fig. 1 of Cheung and Street (1988) (excluding the upward pointing triangles for the reasons explained above), assuming $\varepsilon = 2$ and $\gamma = 2$, as in Teixeira (2012) (Fig. 4a) and using $\varepsilon = 0.5$ and $\gamma = 0.5$ (adjusted values) (Fig. 4b).

It can be seen in Fig. 4a that the behavior of the measured currents is reasonably well reproduced qualitatively, with a decrease of the overall normalized current speed as the wind speed increases. In terms of the input parameters of the model, this is due to a decrease of the turbulent Langmuir number La_t as the wind speed increases for the lowest wind speeds, but mostly due to an increase

477 in penetration of the wave motion at the highest wind speeds, for which La_t actually changes very
478 little (see Table 1). Noteworthy disagreements are that the range of variation of the current speed
479 in the model is much too wide compared with the data, in particular, the current speed in wall
480 coordinates is overestimated for the lowest wind speed and quite underestimated for the highest
481 wind speeds. Additionally, although two logarithmic portions of the current profile exist in the
482 model at the highest wind speeds (lowest values of La_t), these portions do not coincide with the
483 data that show a reduced slope (e.g., stars and open circles). Finally, the detailed variation with
484 the wind speed is not reproduced. While most of the variation occurs at the lowest wind speeds
485 in the model and weakens roughly monotonically as La_t decreases, the rate of variation seems to
486 increase again at the highest wind speeds in the data.

487 When Fig. 4a is compared with Fig. 10 of Kudryavtsev et al. (2008), it may be noticed that the
488 agreement with the data is somewhat less satisfactory. Although the performance of the model of
489 Kudryavtsev et al. (2008) is itself far from perfect, its consideration of the effect of the viscous
490 boundary layer for the current profile with the lowest wind speed substantially improves the agree-
491 ment at small depths compared with the present model. Additionally, the model of Kudryavtsev
492 et al. (2008) does not underestimate the current as much at the highest wind speeds. Curiously, it
493 has some deficiencies similar to those of the present model, namely it overestimates the sensitiv-
494 ity of the normalized current to the wind speed at intermediate values of that parameter and, on
495 the contrary, has a too weak dependence for the highest values. On the other hand, the model of
496 Kudryavtsev et al. (2008) is unable to capture the apparent reduction of u_* by the wave stress, but
497 a somewhat similar effect is mimicked by the transition of the profiles to their viscous boundary
498 layer form (also partly affected by wave breaking).

499 Clearly, the comparison presented in Fig. 4a indicates an overestimation of parameter γ in the
500 present model. One might wonder why this happens, given that this calibration seemed to work

for predictions of the dissipation rate by Teixeira (2012), and also in his preliminary calibration procedure using current profiles from the LES of Li et al. (2005). Possible reasons are speculative, but might have to do with inadvertently accounting for the effect of wave breaking in the first case, and adopting a value of γ suitable for monochromatic waves in the second, both conditions which are not applicable here. It seems fortuitous that both of these distinct differences should lead to a similar value of γ .

In order to improve agreement with the data of Cheung and Street (1988), γ and ε may be readjusted. Figure 4b shows a comparison similar to that of Fig. 4a, but where $\gamma = 0.5$ and $\varepsilon = 0.5$ are assumed, presumably to account for both the absence of wave breaking in the experiments of Cheung and Street (1988) and the fact that the waves are non-monochromatic. The adjusted values of these parameters improve the agreement, particularly for the dataset with the highest wind speed (making it almost perfect by construction), but this turns out not to be sufficient. The variation of the normalized current speed for intermediate wind speeds is still affected by the problems pointed out above.

It is likely that the flow in the experiments under consideration was not always aerodynamically smooth, but rather becomes aerodynamically rough at the highest wind speeds, because of the small-scale corrugations forced at the air-water interface by the wind stress. A form of the roughness length that reflects this is

$$z_0 = c_1 \frac{\nu}{u_*} + c_2 \frac{u_*^2}{g}, \quad (26)$$

where c_1 and c_2 are coefficients, and the second term is of a form analogous to the Charnock relation, but using the friction velocity in the water. In what follows, γ , ε , c_1 and c_2 are adjusted to produce the best possible agreement with the data of Cheung and Street (1988). The values found for the unbounded model are $\gamma = 0.25$, $\varepsilon = 0.5$, $c_1 = 0.2$ and $c_2 = 0.9$.

Figure 5a shows a comparison of the model with the data of Cheung and Street (1988) using these adjusted parameters. The agreement is much better than in Fig. 4, in particular for the rate of variation of the normalized current profiles at intermediate wind speeds (this is not surprising, being a result of the calibration procedure). Agreement is less close for the lowest wind speed considered at small depths, due to the absence of a viscous boundary layer in the model, but this is a minor limitation. The transition of the datasets from a slope corresponding to u_* to the smaller value corresponding to u_{*s} is fairly well reproduced, occurring somewhere around between the wind speeds of 4.7 and 6.7 ms^{-1} . However, at these intermediate wind speeds, the current at the smallest depths covered by the data is somewhat underestimated by the model (the shear suggested by the data at those depths is weaker than expected). Additionally while the current is slightly underestimated for a wind speed of 4.7 ms^{-1} , it is on the contrary slightly overestimated for a wind speed of 3.2 ms^{-1} . It is perhaps risky to attach too much relevance to these discrepancies in detail, given the limited precision of the measurements (which are, nevertheless, among the most precise that could be found).

The value of γ was already discussed above. The value of ε adopted for this comparison would correspond to the Stokes drift of a monochromatic wave with a wavelength 4 times larger than the wavelength of the dominant waves, obtained from the data. The significance of this mismatch for non-monochromatic waves (such as the ones under consideration) is not obvious, but indicates a larger depth of penetration of the wave-induced stress than would be expected. The Stokes drift gradient of a wave spectrum is known to be characterized by a larger penetration depth than a monochromatic wave with the same dominant wavelength (Fig. 18 of Li and Garrett (1993)), and this may perhaps account for a similar effect on the wave-induced stress.

Concerning parameters estimated for (26), $c_1 = 0.2$ is substantially larger than the value of 0.11 most commonly accepted for aerodynamically smooth flow. It is worth noting that, in Fig.

10 of Kudryavtsev et al. (2008) the thin line (corresponding to aerodynamically smooth flow) assumes $z_0 = 0.18\nu/u_*$, which is not too different from the value employed here. Regarding c_2 , the Charnock relation, when expressed in terms of the friction velocity in the airflow, usually has a coefficient of 0.015. Taking into account continuity of the shear stress at the air-water interface, when that relation is expressed in terms of the friction velocity in the water the coefficient should become $833 \times 0.015 = 12.5$. This is clearly much larger than $c_2 = 0.9$ used here, but it should be noted that the Charnock relation, as usually formulated, is valid in the open ocean and for a fully-developed wave field, which are very distinct conditions from those produced in the experiments of Cheung and Street (1988). Additionally, continuity of the shear stress at the air-water interface (used in the above calculation) assumes equilibrium, which is not warranted in these experiments either. Nevertheless, a reassuring aspect is that, on dimensional grounds, the quantities on which (26) depends are still likely to be the most relevant.

It might be argued that the agreement between model and measurements in Fig. 5a was artificially improved by allowing z_0 to vary according to (26). To test this, Fig. 5b shows a similar comparison, but where wave effects are ignored altogether, and only the dependence of z_0 on u_* via (26) is retained (with similar values of c_1 and c_2). It is clear that this dependence, by itself, is unable to produce a satisfactory agreement with the measurements, particularly at the highest wind speeds, and naturally does not represent the decrease of the apparent value of u_* , although it does represent a part of the increase of z_0 required to match the data. Relatedly, (26) contributes significantly to the weakening of the the current speed at the highest wind speeds, which is important to improve agreement with the data relative to Fig. 4.

568 2) FINITE-DEPTH MODEL

569 Figure 6 shows a similar comparison to Fig. 5, but using the finite-depth model developed in
570 section 2c1. Because of the log-linear form of the current profile, the current solutions are no
571 longer composed of straight line segments when using a logarithmic depth scale, but tend to have
572 a reduction in shear at the depths near where the shear stress becomes zero (and the current speed
573 stabilizes), marked by the vertical lines in Fig. 6. Below those levels the shear obviously becomes
574 zero, as is denoted by the horizontal lines in Fig. 6. However, some modified form of the current
575 slope transition at depth $|z| \approx 1/(\epsilon k_w)$ still holds, as can be inferred from Fig. 6, if that depth is
576 above the level where the shear stress vanishes (which always happens in the data of Cheung and
577 Street (1988) – see Table 1). The parameter values used in Fig. 6 are $\gamma = 0.25$, $\epsilon = 1$, $c_1 = 0.2$ and
578 $c_2 = 0.9$. The agreement between the model and measurements is roughly as satisfactory as in Fig.
579 5, with essentially the same deficiencies in the mid-range of wind speeds. At the largest depths
580 considered (near to $|z| = \delta$) the model tends to underestimate the measurements more, perhaps
581 because the reduction of shear in those regions is too large due to the assumption of a linearly
582 decreasing shear stress. In reality, the fact that the shear stress decays to zero more gradually
583 might explain why no marked reduction in the shear is detectable in the data at those depths. The
584 existence of this shear reduction in the model counteracts the transition to a larger shear that occurs
585 below the depth $|z| \approx 1/(\epsilon k_w)$, when this is not too distant from $|z| = \delta$. This is what allows a
586 larger value of ϵ to be employed in Fig. 6.

587 A noteworthy property of this finite-depth model is that it enables an estimation of the magnitude
588 of the surface current speed U_0 , as noted in section 2c1. Figure 7 shows a comparison of the values
589 of U_0/u_* calculated from the model (corresponding to the horizontal portions of the curves in Fig.
590 6) with the values that can be either obtained directly from Table 1 of Cheung and Street (1988)

(circles), or obtained from the data point with the largest depth in the datasets for each wind speed in Fig. 6 (triangles). It can be seen that the agreement is encouraging, with correlation coefficients of ≈ 0.95 in both cases, although the model does tend to systematically underestimate the data. However, given the strong assumptions adopted, the agreement is surprisingly good.

4. Concluding remarks

This study presents a simple model for the wind-driven current existing in the oceanic boundary layer in the presence of surface waves generated by the wind. The model sheds light on two puzzling aspects that have been noted repeatedly about these currents, for which a logarithmic profile model, with the friction velocity u_* and roughness length z_0 as basic parameters, has often been adopted. Firstly, if the current speed is scaled using the total friction velocity, measured independently, e.g., using the surface wind stress, the friction velocity diagnosed from shear in the current profile is smaller than expected, being only a fraction of the total friction velocity. Secondly, the roughness length diagnosed from the same fitting procedure is much larger than expected, by various orders of magnitude, being inconsistent with the roughness length that would be estimated either for an aerodynamically smooth flow, or aerodynamically rough flow affected by waves. The corresponding Charnock parameter appears to be enormously amplified (Bourassa 2000).

Both of these features are explained here as resulting from a partition of the total turbulent shear stress into a shear-induced component and a wave-induced component, which result from the local mechanical production of this stress by the mean shear in the current profile, and by the Lagrangian strain rate associated Stokes drift of the waves, respectively, when the effect of non-breaking waves is included in the equations of motion via the Craik-Leibovich vortex force. In this framework, the wave-associated part of the shear stress is not a property of the wave itself, as assumed by some

614 authors, but is a stress created, on the turbulence that co-exists with the shear-induced stress, by
615 Stokes drift straining of turbulent vorticity into the streamwise direction (the assumed direction
616 of both the mean current and the Stokes drift) (Teixeira 2011a). This is independent from any
617 vertical mixing associated with pre-existing turbulence, or turbulence injected into the water by
618 wave breaking.

619 It is likely that this mechanism associated with non-breaking waves acts in concert with other
620 mechanisms related to wave breaking, and with the transport of turbulence by itself in general, but
621 the fact that it can account for the two phenomena mentioned above, and that its dependence on
622 the turbulent Langmuir number appears to be confirmed by measurements, support its relevance.

623 The model predicts that the part of the turbulent shear stress induced by shear in the surface
624 layer becomes a progressively smaller fraction of the total stress near the surface and down to a
625 depth of the order the wavelength of the dominant surface waves as La_t decreases. This leads to
626 the perceived reduction of the friction velocity. The model also predicts that the roughness length
627 inferred if the uppermost portion of the current profile is disregarded is amplified by various orders
628 of magnitude as La_t decreases, and scales with k_w^{-1} , i.e., the wavelength of the waves, at small La_t .
629 The profile of the wind-induced current becomes flatter (that is, less different from its surface
630 value) as La_t decreases.

631 If the parameters in the model are adjusted appropriately, departing from their values assumed
632 in Teixeira (2012) (presumably to account for the facts that there is no substantial wave break-
633 ing in the experiments and the waves are not monochromatic), good agreement is found with the
634 laboratory measurements of Cheung and Street (1988), which appear to be the only dataset that
635 is precise and comprehensive enough for this purpose. Other more recent datasets (Siddiqui and
636 Loewen 2007, Longo et al. 2012) either seem unreliable, or do not provide complete enough infor-
637 mation about the characteristics of the wave field or of the total shear stress. In the experiments of

638 Cheung and Street (1988), the current profile becomes flatter as the wind speed increases. Using
639 the present model, this is interpreted as being primarily due to a decrease in La_t at the lowest wind
640 speeds, and due to an increasingly deeper penetration of the wave stress, conjugated with a higher
641 real roughness length, at the highest wind speeds.

642 As in the present model, a recent study of Sinha et al. (2015) uses insights from Teixeira (2012)
643 to develop a turbulence closure that includes wave effects. However, the dataset they use to test
644 their model, from LES of Tejada-Martinez et al. (2013), refers to shallow water flow, and is thus
645 strongly affected by the bottom boundary layer. Sinha et al. (2015) primarily focus on an analysis
646 of the current profile in wall-coordinates within the bottom boundary layer, but the full-depth
647 current profiles shown by them (e.g., their Figs. 19 and 21) suggest a relatively modest agreement
648 between their model in the top boundary layer adjacent to the air-water interface, despite the fact
649 that they include a term in the shear stress definition that is non-local, accounting for turbulent
650 transport of TKE (which is not considered here).

651 In order to bring the model presented here closer to real oceanic conditions, and thus increase its
652 usefulness, it is probably not only necessary to account for non-local mixing (which is important
653 in some datasets), but also for the effect of the Earth's rotation, as wind-driven currents are known
654 to be typically misaligned with the surface stress and rotate with depth, in accordance with Ekman
655 layer theory. However, within the surface layer where the shear stress is the primary mechanism
656 shaping the current, shear at least is necessarily aligned with the wind stress, and thus the model
657 presented here may still be directly applicable to the streamwise component of the current.

658 Defining precisely the range of applicability of the present model is complicated (when com-
659 pared to the atmosphere) by the presence of surface waves, as their influence may in some cases
660 be confined to the oceanic surface layer (as happens here), and in others extend below it. To a first

661 approximation, the surface layer might be defined as the layer in which there is little fractional
662 change in the vertical of both the shear stress and the current direction.

663 The results reported here are presented in dimensionless form, which should facilitate their trans-
664 position to real oceanic conditions, enabling the development of physically-based parametrizations
665 for the turbulent momentum flux in the wave-affected boundary layer for ocean circulation models.

666 References

667 Agrawal, Y. C., E. A. Terray, M. A. Donelan, P. A. Hwang, A. J. W. III, W. M. Drennan, K. K.
668 Kahma, and S. A. Kitaigorodskii, 1992: Enhanced dissipation of kinetic energy beneath surface
669 waves. *Nature*, **359**, 219–220.

670 Bourassa, M. A., 2000: Shear stress model for the aqueous boundary layer near the air-water
671 interface. *J. Geophys. Res.*, **105**, 1167–1176.

672 Burchard, H., 2001: Simulating the wave-enhanced layer under breaking surface waves with two-
673 equation turbulence models. *J. Phys. Oceanogr.*, **31**, 3133–3145.

674 Cheung, T. K., and R. L. Street, 1988: The turbulent layer in the water at an air-water interface. *J.*
675 *Fluid Mech.*, **194**, 133–151.

676 Craig, P. D., 1996: Velocity profiles and surface roughness under breaking waves. *J. Geophys.*
677 *Res.*, **101**, 1265–1277.

678 Craig, P. D., and M. L. Banner, 1994: Modeling wave-enhanced turbulence in the ocean surface
679 layer. *J. Phys. Oceanogr.*, **24**, 2546–2559.

680 Csanady, G. T., 1984: The free surface turbulent shear layer. *J. Phys. Oceanogr.*, **14**, 402–411.

- 681 Csanady, G. T., 2004: *Air-Sea Interaction - Laws and Mechanisms*. Cambridge University Press,
682 239 pp.
- 683 Drennan, W. M., M. A. Donelan, E. A. Terray, and K. B. Katsaros, 1996: Oceanic turbulence
684 dissipation measurements in swade. *J. Phys. Oceanogr.*, **26**, 808–815.
- 685 Feddersen, F., J. H. Trowbridge, and A. J. W. III, 2007: Vertical structure of dissipation in the
686 nearshore. *J. Phys. Oceanogr.*, **37**, 1764–1777.
- 687 Gargett, A. E., 1989: Ocean turbulence. *Ann. Rev. Fluid Mech.*, **21**, 419–451.
- 688 Gemmrich, J. R., and D. M. Farmer, 1999: Near-surface turbulence and thermal structure in a
689 wind-driven sea. *J. Phys. Oceanogr.*, **29**, 480–499.
- 690 Gerbi, G. P., J. H. Trowbridge, E. A. Terray, A. J. Plueddemann, and T. Kukulka, 2009: Observations
691 of turbulence in the ocean surface boundary layer: energetics and transport. *J. Phys. Oceanogr.*,
692 **39**, 1077–1096.
- 693 Grant, A. L. M., and S. E. Belcher, 2009: Characteristics of langmuir turbulence in the ocean
694 mixed layer. *J. Phys. Oceanogr.*, **39**, 1871–1887.
- 695 Harcourt, R. R., 2013: A second-moment closure model of langmuir turbulence. *J. Phys.*
696 *Oceanogr.*, **43**, 673–697.
- 697 Howe, B. M., A. J. Chambers, S. P. Klotz, T. K. Cheung, and R. L. Street, 1982: Comparison of
698 profiles and fluxes of heat and momentum above and below an air-water interface. *Trans. ASME*
699 *C: J. Heat Transfer*, **104**, 34–39.
- 700 Jones, N. L., and S. G. Monismith, 2008: The influence of whitecapping waves on the vertical
701 structure of turbulence in a shallow estuarine embayment. *J. Phys. Oceanogr.*, **38**, 1563–1580.

702 Kondo, J., 1976: Parameterization of turbulent transport in the top meter of the ocean. *J. Phys.*
703 *Oceanogr.*, **6**, 712–720.

704 Kraus, E. B., and J. A. Businger, 1994: *Atmosphere-Ocean Interaction, Second Edition*. Oxford
705 University Press, 362 pp.

706 Kudryavtsev, V., V. Shrira, V. Dulov, and V. Malinovsky, 2008: On the vertical structure of wind-
707 driven sea currents. *J. Phys. Oceanogr.*, **38**, 2121–2144.

708 Kukulka, T., and R. R. Harcourt, 2017: Influence of stokes drift decay scale on langmuir turbu-
709 lence. *J. Phys. Oceanogr.*, **47**, 1637–1656.

710 Kukulka, T., A. J. Plueddemann, J. H. Trowbridge, and P. P. Sullivan, 2010: Rapid mixed
711 layer deepening by the combination of langmuir and shear instabilities: a case study. *J. Phys.*
712 *Oceanogr.*, **40**, 2381–2400.

713 Lee, M. J., J. Kim, and P. Moin, 1990: Structure of turbulence at high shear rate. *J. Fluid Mech.*,
714 **216**, 561–583.

715 Li, M., and C. Garrett, 1993: Cell merging and the jet/downwelling ratio in langmuir circulation.
716 *J. Marine Res.*, **51**, 737–769.

717 Li, M., C. Garrett, and E. Skillingstad, 2005: A regime diagram for classifying turbulent large
718 eddies in the upper ocean. *Deep-Sea Res.*, **52**, 259–278.

719 Longo, S., D. Liang, L. Chiapponi, and L. A. Jiménez, 2012: Turbulent flow structure in experi-
720 mental laboratory wind-generated gravity waves. *Coastal. Eng.*, **64**, 1–15.

721 McLeish, W. L., and G. E. Putland, 1975: Measurements of wind-driven flow profiles in the top
722 millimeter of water. *J. Phys. Oceanogr.*, **5**, 516–518.

723 McWilliams, J. C., P. P. Sullivan, and C.-H. Moeng, 1997: Langmuir turbulence in the ocean. *J.*
724 *Fluid Mech.*, **334**, 1–30.

725 Pearson, B., 2018: Turbulence-induced anti-stokes flow and the resulting limitations of large-eddy
726 simulation. *J. Phys. Oceanogr.*, **48**, 117–122.

727 Phillips, O. M., 1977: *The Dynamics of the Upper Ocean*. Cambridge University Press, 336 pp.

728 Polton, J. A., and S. E. Belcher, 2007: Langmuir turbulence and deeply penetrating jets in an
729 unstratified mixed layer. *J. Geophys. Res.*, **112**, C09 020.

730 Polton, J. A., D. M. Lewis, and S. E. Belcher, 2005: The role of wave-induced coriolis-stokes
731 forcing on the wind-driven mixed layer. *J. Phys. Oceanogr.*, **35**, 444–457.

732 Rascle, N., and F. Ardhuin, 2009: Drift and mixing under the ocean surface revisited: stratified
733 conditions and model-data comparisons. *J. Geophys. Res.*, **114**, C02 016.

734 Rascle, N., F. Ardhuin, and E. A. Terray, 2006: Drift and mixing under the ocean surface: a
735 coherent one-dimensional description with application to unstratified conditions. *J. Geophys.*
736 *Res.*, **111**, C03 016.

737 Siddiqui, M. H. K., and M. R. Loewen, 2007: Characteristics of the wind drift layer and microscale
738 breaking waves. *J. Fluid Mech.*, **573**, 417–456.

739 Sinha, N., A. E. Tejada-Martinez, C. Akan, and C. E. Grosch, 2015: Toward a k-profile parameter-
740 ization of langmuir turbulence in shallow coastal shelves. *J. Phys. Oceanogr.*, **45**, 2869–2895.

741 Soloviev, A., and R. Lukas, 2003: Observation of wave-enhanced turbulence in the near-surface
742 layer of the ocean during toga coare. *Deep-Sea Res.*, **50**, 371–395.

743 Sullivan, P. P., J. C. McWilliams, and W. K. Melville, 2004: The oceanic boundary layer driven by
 744 wave breaking with stochastic variability. part 1. direct numerical simulations. *J. Fluid Mech.*,
 745 **507**, 143–174.

746 Teixeira, M. A. C., 2011a: A linear model for the structure of turbulence beneath surface water
 747 waves. *Ocean Modell.*, **36**, 149–162.

748 Teixeira, M. A. C., 2011b: On the connection between dissipation enhancement in the ocean
 749 surface layer and langmuir circulations. *J. Phys. Oceanogr.*, **41**, 2000–2007.

750 Teixeira, M. A. C., 2012: The influence of langmuir turbulence on the scaling for the dissipation
 751 rate in the oceanic boundary layer. *J. Geophys. Res.*, **117**, C05 015.

752 Teixeira, M. A. C., and S. E. Belcher, 2002: On the distortion of turbulence by a progressive
 753 surface wave. *J. Fluid Mech.*, **458**, 229–267.

754 Teixeira, M. A. C., and S. E. Belcher, 2010: On the structure of langmuir turbulence. *Ocean*
 755 *Modell.*, **31**, 105–119.

756 Tejada-Martinez, A. E., C. Akan, C. E. G. N. Sinha, and G. Martinat, 2013: Surface dynamics in
 757 les of full-depth langmuir circulation in shallow water. *Phys. Scr.*, **T155**, 014 008.

758 Terray, E. A., M. A. Donelan, Y. C. Agrawal, W. M. Drennan, K. K. Kahma, A. J. W. III, P. A.
 759 Hwang, and S. A. Kitaigorodskii, 1996: Estimates of kinetic energy dissipation under breaking
 760 waves. *J. Phys. Oceanogr.*, **26**.

761 Terray, E. A., W. M. Drennan, and M. A. Donelan, 1999: The vertical structure of shear and
 762 dissipation in the ocean surface layer. *Proc. Synp. on the Wind-driven Air-Sea Interface-*
 763 *Electromagnetic and Acoustic Sensing, Wave Dynamics and Turbulent Fluxes*, Sydney, Aus-
 764 tralia, University of New South Waves, 239–245.

765 Thorpe, S. A., 2005: *The turbulent ocean*. Cambridge University Press, 439 pp.

766 Van Roekel, L. P., B. Fox-Kemper, P. P. Sullivan, P. E. Hamlington, and S. R. Haney, 2012: The
767 form and orientation of langmuir cells for misaligned winds and waves. *J. Geophys. Res.*, **117**,
768 C05 001.

769
770
771
772
773
774
775
776
777

LIST OF TABLES

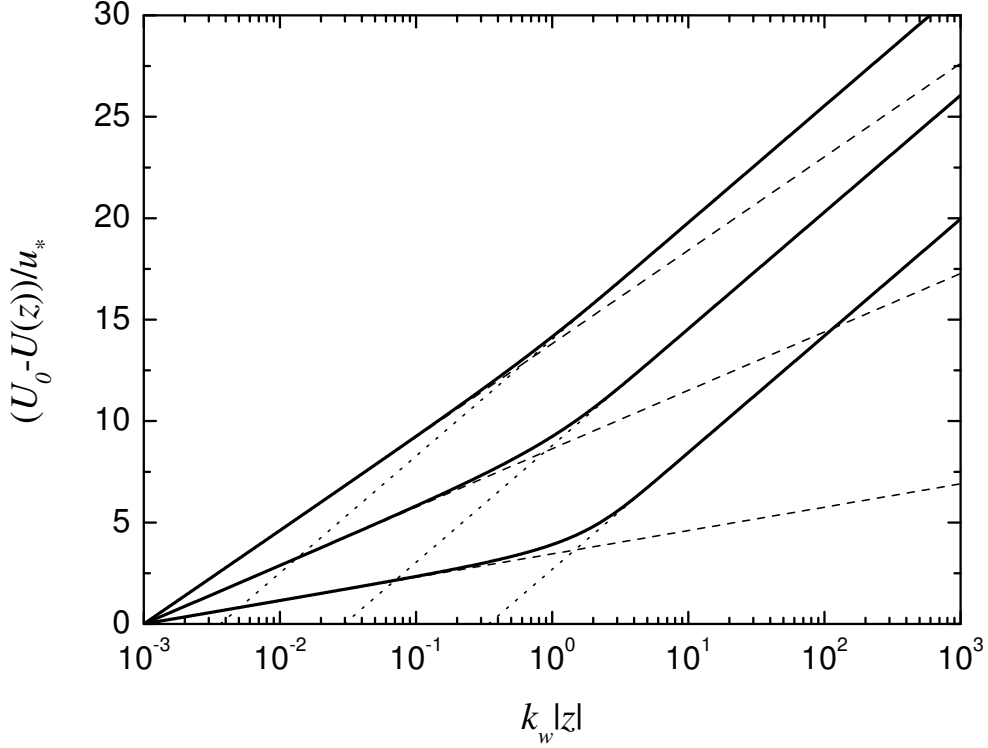
Table 1. Parameters of the datasets from Cheung and Street (1988) used here, and derived parameters: wind speed, depth of the boundary layer δ , wavelength of the dominant waves λ_w , depth of penetration of the wave stress $1/(\epsilon k_w)$, surface Stokes drift velocity $U_S(z = 0)$, and turbulent Langmuir number La_t . $1/(\epsilon k_w)$, $U_S(z = 0)$ and La_t were estimated from the dominant wave parameters using a monochromatic wave approximation (see text). $1/(\epsilon k_w)$ is estimated for the cases displayed in Figs. 4b and 5a, where $\epsilon = 0.5$ (the lowest value of ϵ considered). For other cases, ϵ must be changed accordingly. 37

TABLE 1. Parameters of the datasets from Cheung and Street (1988) used here, and derived parameters: wind speed, depth of the boundary layer δ , wavelength of the dominant waves λ_w , depth of penetration of the wave stress $1/(\varepsilon k_w)$, surface Stokes drift velocity $U_S(z=0)$, and turbulent Langmuir number La_t . $1/(\varepsilon k_w)$, $U_S(z=0)$ and La_t were estimated from the dominant wave parameters using a monochromatic wave approximation (see text). $1/(\varepsilon k_w)$ is estimated for the cases displayed in Figs. 4b and 5a, where $\varepsilon = 0.5$ (the lowest value of ε considered). For other cases, ε must be changed accordingly.

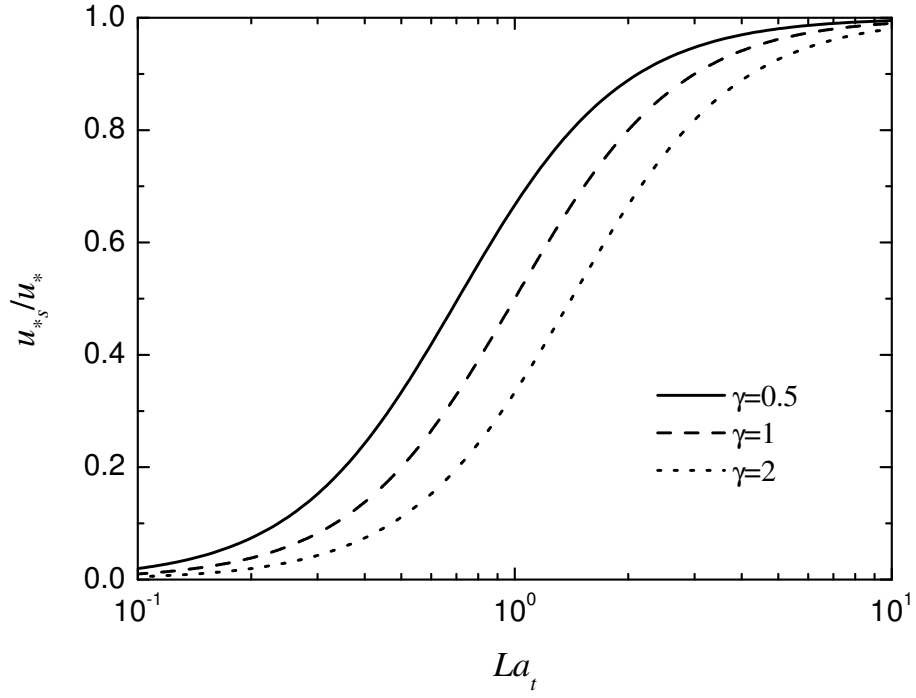
Windspeed (m s^{-1})	δ (cm)	λ_w (cm)	$1/(\varepsilon k_w)(\varepsilon = 0.5)$ (cm)	$U_S(z=0)(\text{cm s}^{-1})$	La_t
2.6	31.0	4.2	1.3	0.015	4.7
3.2	34.8	5.8	1.8	0.98	0.71
4.7	26.4	12.7	4.1	2.6	0.52
6.7	24.9	21.4	6.8	4.1	0.53
9.9	35.4	27.1	8.6	6.0	0.54
13.1	29.8	39.0	12.4	9.7	0.53

LIST OF FIGURES

- Fig. 1.** Normalized current speed as a function of normalized depth for different values of La_t , calculated from (15) for $\gamma = 1$, $\varepsilon = 1$ and $k_w z_0 = 0.001$. Solid lines: current profiles, for $La_t = 2$, $La_t = 1$ and $La_t = 0.5$ (from top to bottom). Dashed lines: extension of the asymptotes (with slope $(u_{*s}/u_*)/\kappa$) corresponding to the currents at small depths to large depths. Dotted lines: extension of the asymptotes (with slope $1/\kappa$) corresponding to the currents at large depths up to the depths where the currents would be zero, corresponding to the values of the apparent roughness length $k_w z_{0w}$ 39
- Fig. 2.** Ratio of the shear-associated friction velocity to the total friction velocity as a function of La_t for different values of γ , calculated from (9). See legend for meaning of different line types. 40
- Fig. 3.** Normalized apparent roughness length as a function of La_t for $\gamma = 1$ and $\varepsilon = 1$ from (21), for different values of $k_w z_0$. (a) Apparent roughness length normalized by k_w , (b) ratio of apparent to true roughness length. See legend for meaning of different line types. 41
- Fig. 4.** Comparison between normalized current speed profiles in wall-coordinates from the model developed here, given by (16) or (17) (lines), and from the measurements of Cheung and Street (1988) (symbols), for different wind speeds. The model assumes $c_1 = 0.11$ and $c_2 = 0$ in (26). Solid line and filled circles: 2.6 m s^{-1} , dashed line and squares: 3.2 m s^{-1} , dotted line and triangles: 4.7 m s^{-1} , dash-dotted line and diamonds: 6.7 m s^{-1} , dash-double-dotted line and stars: 9.9 m s^{-1} , short-dotted line and open circles: 13.1 m s^{-1} . (a) $\gamma = 2$ and $\varepsilon = 2$, (b) $\gamma = 0.5$ and $\varepsilon = 0.5$ 42
- Fig. 5.** Similar to Fig. 4, but for $c_1 = 0.2$ and $c_2 = 0.9$ in (26), and different values of γ and ε . (a) $\gamma = 0.25$ and $\varepsilon = 0.5$, (b) $\gamma = 0$ (i.e., no wave effects). 43
- Fig. 6.** Similar to Fig. 5, but using the finite-depth model for which the shear stress decreases linearly with depth (24), with $\gamma = 0.25$, $\varepsilon = 1$, $c_1 = 0.2$ and $c_2 = 0.9$. The vertical lines (same type as the corresponding current profiles) denote the depths at which the shear stress reaches zero in each case ($z^+ = \delta u_*/\nu$). Note that the current profiles for larger depths remain constant in the model 44
- Fig. 7.** Normalized current speed at the surface predicted by the finite-depth model (24) (for $z^+ = \delta u_*/\nu$) as a function of corresponding values derived from the measurements. Circles: measured values taken directly from Table 1 of Cheung and Street (1988), triangles: measured values taken as the data point at the largest depth from the datasets corresponding to each different wind speed. 45



817 FIG. 1. Normalized current speed as a function of normalized depth for different values of La_t , calculated from
 818 (15) for $\gamma = 1$, $\varepsilon = 1$ and $k_w z_0 = 0.001$. Solid lines: current profiles, for $La_t = 2$, $La_t = 1$ and $La_t = 0.5$ (from
 819 top to bottom). Dashed lines: extension of the asymptotes (with slope $(u_{*s}/u_*)/\kappa$) corresponding to the currents
 820 at small depths to large depths. Dotted lines: extension of the asymptotes (with slope $1/\kappa$) corresponding to the
 821 currents at large depths up to the depths where the currents would be zero, corresponding to the values of the
 822 apparent roughness length $k_w z_{0w}$.



823 FIG. 2. Ratio of the shear-associated friction velocity to the total friction velocity as a function of La_t for
824 different values of γ , calculated from (9). See legend for meaning of different line types.

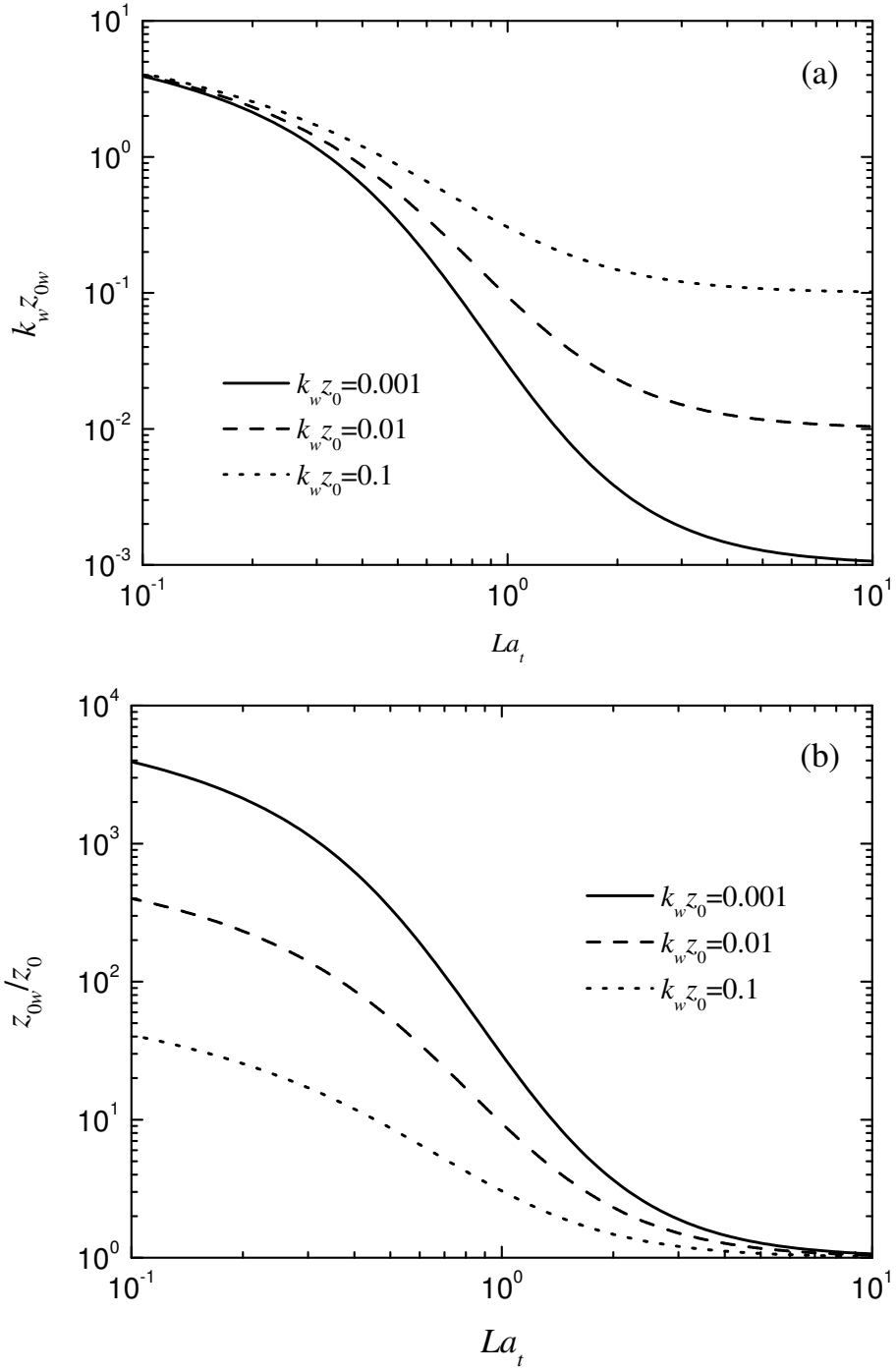
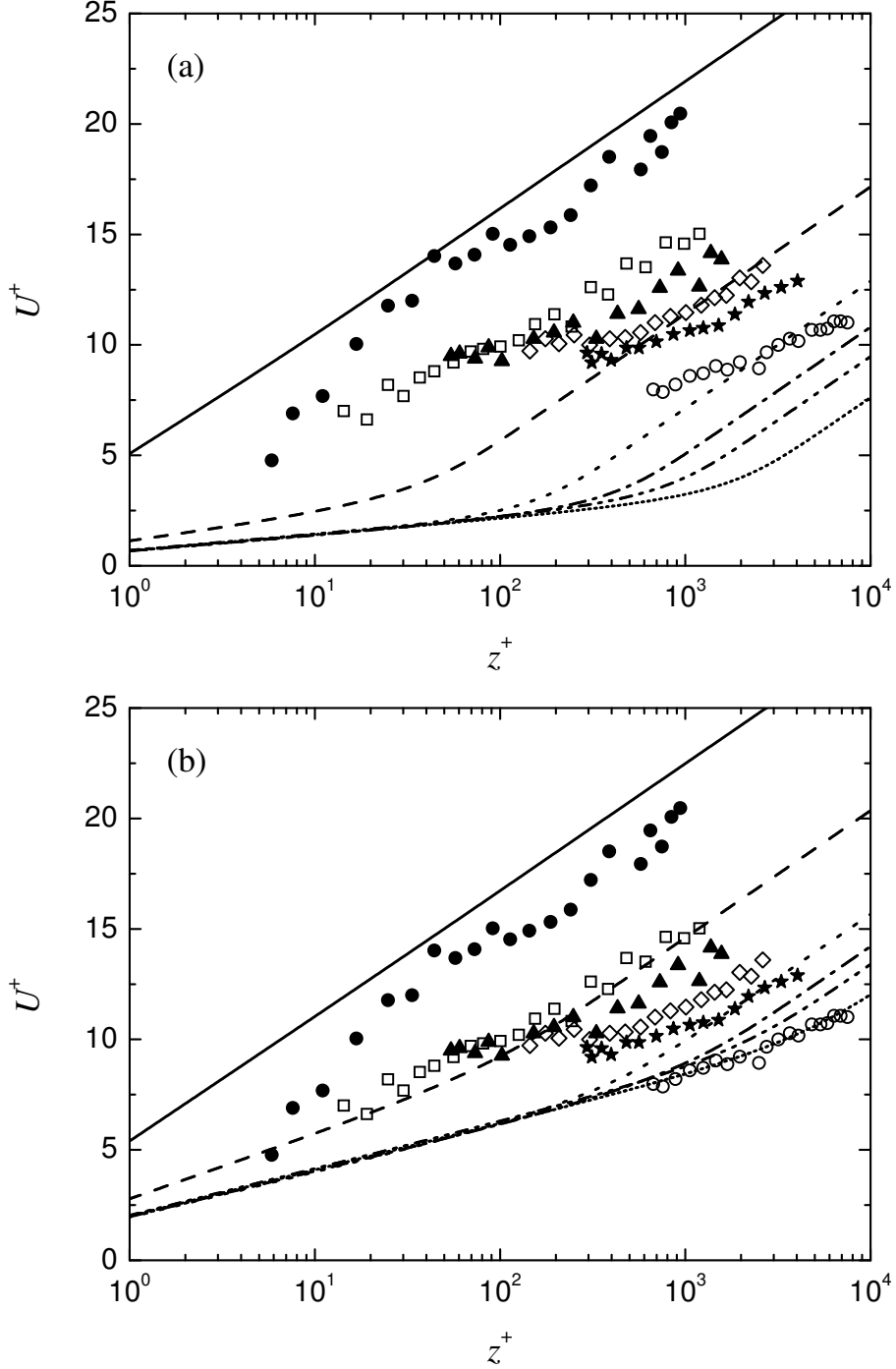


FIG. 3. Normalized apparent roughness length as a function of La_t for $\gamma = 1$ and $\varepsilon = 1$ from (21), for different values of $k_w z_0$. (a) Apparent roughness length normalized by k_w , (b) ratio of apparent to true roughness length. See legend for meaning of different line types.



828 FIG. 4. Comparison between normalized current speed profiles in wall-coordinates from the model developed
 829 here, given by (16) or (17) (lines), and from the measurements of Cheung and Street (1988) (symbols), for differ-
 830 ent wind speeds. The model assumes $c_1 = 0.11$ and $c_2 = 0$ in (26). Solid line and filled circles: 2.6 m s^{-1} , dashed
 831 line and squares: 3.2 m s^{-1} , dotted line and triangles: 4.7 m s^{-1} , dash-dotted line and diamonds: 6.7 m s^{-1} , dash-
 832 double-dotted line and stars: 9.9 m s^{-1} , short-dotted line and open circles: 13.1 m s^{-1} . (a) $\gamma = 2$ and $\varepsilon = 2$, (b)
 833 $\gamma = 0.5$ and $\varepsilon = 0.5$.

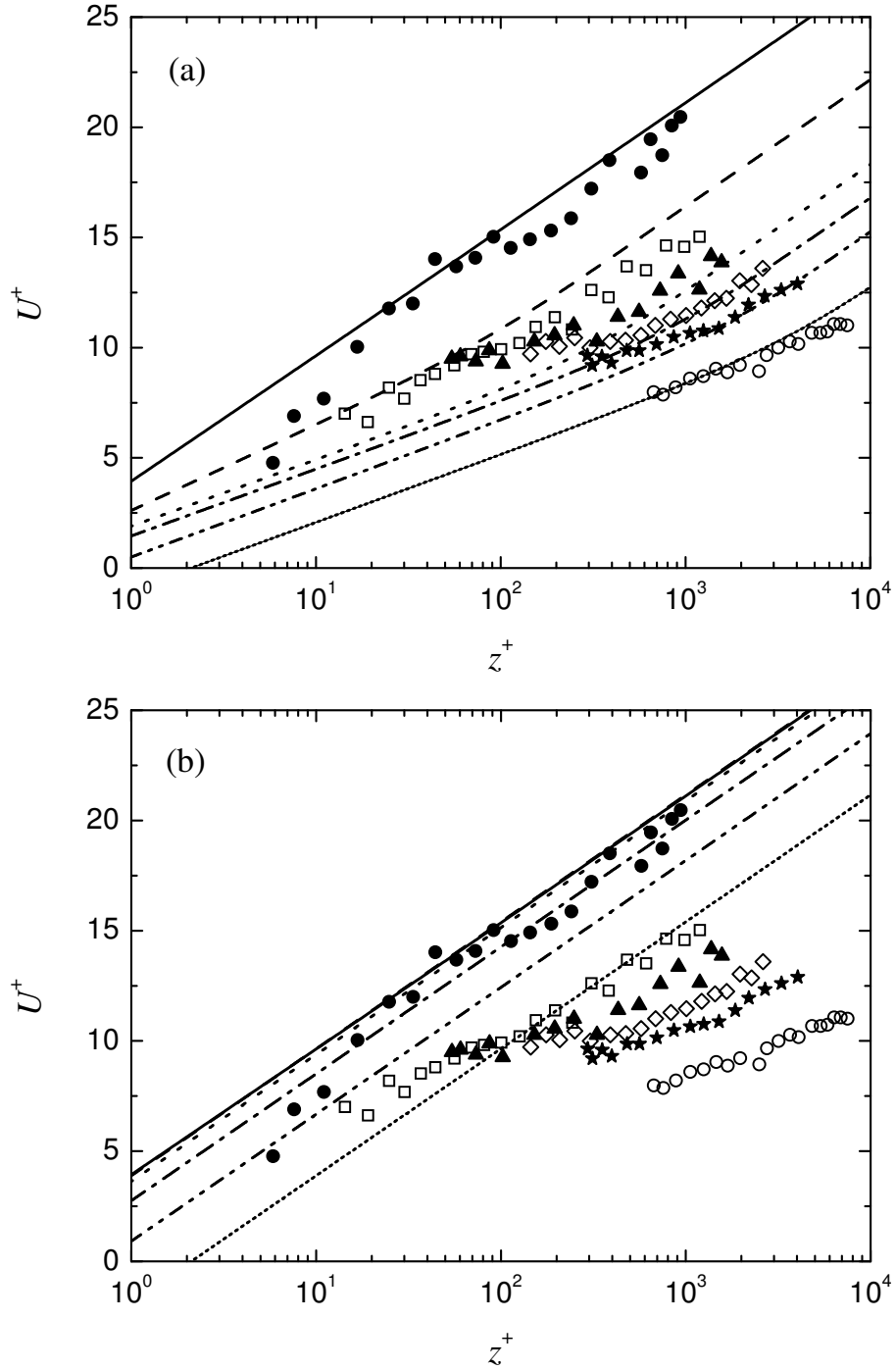
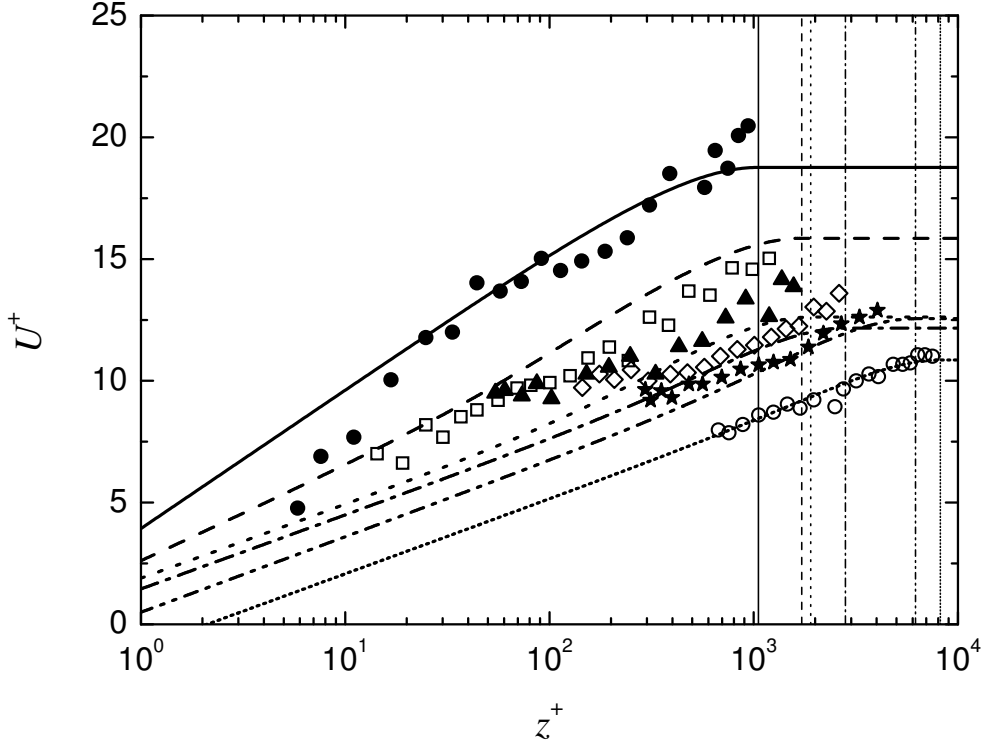
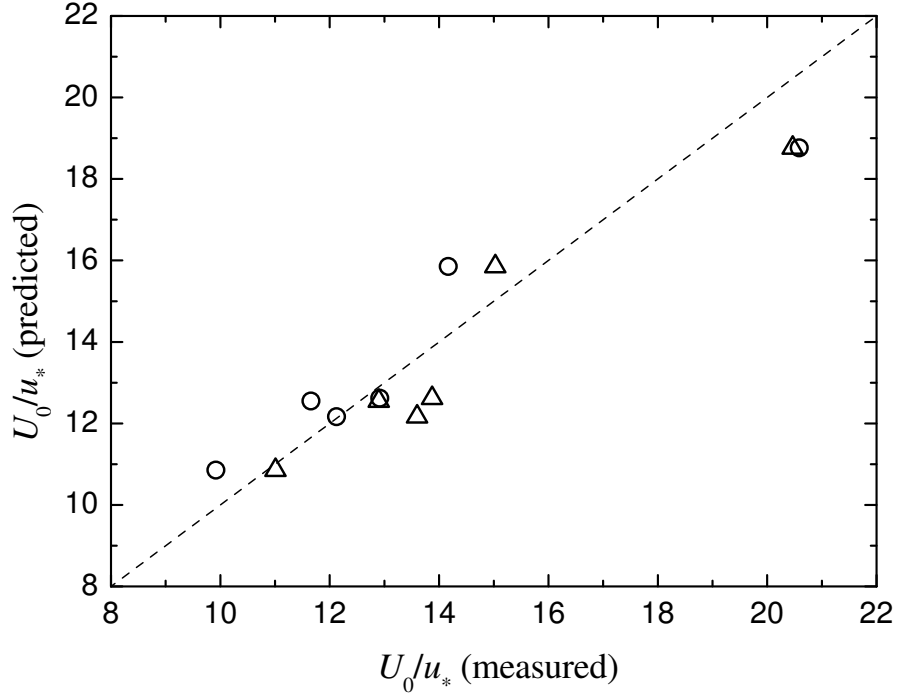


FIG. 5. Similar to Fig. 4, but for $c_1 = 0.2$ and $c_2 = 0.9$ in (26), and different values of γ and ϵ . (a) $\gamma = 0.25$ and $\epsilon = 0.5$, (b) $\gamma = 0$ (i.e., no wave effects).



836 FIG. 6. Similar to Fig. 5, but using the finite-depth model for which the shear stress decreases linearly with
 837 depth (24), with $\gamma = 0.25$, $\varepsilon = 1$, $c_1 = 0.2$ and $c_2 = 0.9$. The vertical lines (same type as the corresponding
 838 current profiles) denote the depths at which the shear stress reaches zero in each case ($z^+ = \delta u_* / \nu$). Note that
 839 the current profiles for larger depths remain constant in the model



840 FIG. 7. Normalized current speed at the surface predicted by the finite-depth model (24) (for $z^+ = \delta u_*/\nu$)
 841 as a function of corresponding values derived from the measurements. Circles: measured values taken directly
 842 from Table 1 of Cheung and Street (1988), triangles: measured values taken as the data point at the largest depth
 843 from the datasets corresponding to each different wind speed.